Physics – Uspekhi **68** (10) 987 – 1000 (2025)

REVIEWS OF TOPICAL PROBLEMS

PACS numbers: **07.87.+v**, 98.70.Vc, 98.80.Es

New horizons for research on cosmic microwave background

D.I. Novikov, A.G. Doroshkevich, T.I. Larchenkova, A.M. Malinovsky, A.O. Mihalchenko, A.M. Osipova, K.O. Parfenov, S.V. Pilipenko

DOI: https://doi.org/10.3367/UFNe.2025.08.040006

Contents

Abstract. Despite the significant progress achieved since the turn of the century in the study of the cosmic microwave background (CMB), several major problems facing modern observational cosmology remain unsolved. They include proving or disproving the inflationary theory of the evolution of the Universe and its thermal history in the pre-recombination period. The power spectrum of the initial perturbations on small scales also remains unknown. A detailed study of the CMB polarization and its frequency spectrum will shed light on these pressing questions, many of which cannot be answered based on any observations other than those of the CMB. Resolving these problems, as a by-product, will provide new information on the properties of foreground radiation (dust emission, cosmic infrared background, synchrotron radiation, free–free emission, and CO lines) and gravitational lensing. Next-generation experiments aim to address the above-mentioned problems in observational cosmology.

Keywords: cosmic microwave background, CMB polarization, spectral distortions, foreground separation, B-mode

D.I. Novikov [1,a], **A.G. Doroshkevich** [1,b], **T.I. Larchenkova** [1,c], **A.M. Malinovsky** [1,d], **A.O. Mihalchenko** [1,e], **A.M. Osipova** [1,2,f], **K.O. Parfenov** [1,g], **S.V. Pilipenko** [1,h]

[1] Lebedev Physical Institute, Russian Academy of Sciences, Leninskii prosp. 53, 119991 Moscow, Russian Federation

[2] HSE University, ul. Myasnitskaya 20, 101000 Moscow, Russian Federation

E-mail: [a] novikovdi@lebedev.ru, [b] dorr@asc.rssi.ru, [c] ltanya@asc.rssi.ru, [d] Ingirami@gmail.com, [e] mihalchenko.ao@asc.rssi.ru, [f] osipova@asc.rssi.ru, [g] k.o.parfenov@asc.rssi.ru, [h] s.pilipenko@asc.rssi.ru

Received 12 January 2025, revised 14 August 2025
Uspekhi Fizicheskikh Nauk **195** (10) 1047 – 1061 (2025)
Translated by S. Alekseev

1. Introduction

The cosmic microwave background (CMB) is a vital source of information about the structure of the Universe and its evolution at all stages, including inflation, the pre-recombination epoch, recombination, reionization, and the formation of the large-scale structure. Over the past decades, the global scientific community has made significant progress in studying the CMB. Observations by the recent WMAP [1] and Planck [2, 3] space missions have significantly expanded our knowledge of the anisotropy and polarization properties of the CMB on scales down to a few arcminutes, measured the angular spectrum with high precision, and discovered a distribution of temperature fluctuations in the CMB and its polarization features that was very close to Gaussian. All this has brought us closer to refining the fundamental parameters of the Standard Cosmological Model and understanding the evolution of the Universe [4].

However, the two main unresolved problems of modern observational cosmology remain the detection of the primordial B-mode polarization of the CMB and the refinement of its frequency spectrum.

• Primordial B-mode polarization.

Detection of the primordial B-mode polarization of the CMB will provide direct evidence for the inflationary theory of the evolution of the Universe. However, the extremely small ratio r of the tensor-mode to scalar-mode perturbation amplitudes, the presence of polarized foregrounds, gravitational lensing, power leakage from temperature anisotropy to polarization during observations, and the inevitable power transfer from the E- to B-mode due to incomplete sky coverage in some experiments and the discrete nature of observational data make it difficult to detect the B-mode generated during inflation. Future experiments such as SO [5], LiteBIRD [6], and PIXIE [7] aim to detect the B-mode or

to place an upper bound on its amplitude down to $r \sim 0.01$, 0.001. Clearly, in addition to improving the sensitivity of experiments and expanding the frequency ranges of observations, it is necessary to develop methods suitable for processing observational data to overcome these difficulties. The main approaches here are multifrequency [8, 9] and spatial–statistical [10] analyses, which, to a certain extent, allow the separation of components with different frequency spectra or significantly different correlation characteristics. Careful modeling of spatial–correlation features is also important for removing distortions caused by gravitational lensing from the signal [11–14].

We note that, given the limited sensitivity of experiments, these approaches are insufficient for reliably detecting the cosmological B-mode. An approach to processing observational data based on the key feature of inflation — the creation of perturbations corresponding to Gaussian statistics — is crucial [15, 16]. Therefore, based on the statistical properties of the signal, it is desirable to be able to separate the Gaussian part of the observational data from the non-Gaussian part. Furthermore, methods for testing random fields for Gaussianity that are sensitive to the presence of specific non-Gaussian polarized foregrounds are needed.

• Spectral distortions.

The discovery of deviations in the CMB spectrum from the blackbody distribution [17–19] reveals a wealth of information about the thermal history of the Universe, both in the pre-recombination epoch and during the formation of galaxies. More than 30 years ago, the COBE/FIRAS experiment [20, 21] established with high precision that the CMB frequency spectrum corresponds to a blackbody distribution with temperature $T = 2.72548$ K. Since then, no significant steps have been made towards refining the features of this spectrum. At the same time, the detection of deviations of the CMB spectrum from the blackbody spectrum is considered one of the main tasks of modern cosmology. Of the most interest and promise is the study of so-called μ-distortions of the spectrum from the blackbody distribution. Such spectral features arise at an early stage of evolution as a result of the violation of thermodynamic equilibrium between cosmic plasma and radiation at redshifts in the range from $z \sim 2 \times 10^6$ to $z \sim 10^4$. The reason for such a change in the spectrum may be an injection of energy into the plasma or a change in the number of photons per unit volume. Consequently, a Bose–Einstein spectrum with a nonzero chemical potential $\mu \sim 10^{-8}$ emerges instead of the Planck distribution. Due to the homogeneity and isotropy of the Universe on large scales, one can expect that this kind of distortion will be the same in all directions, like the CMB radiation itself.

Thus, in the presence of a nonzero monopole component of μ-distortions, the CMB spectrum is determined not by a single constant — the temperature T of the CMB (which is the temperature of our Universe) — but by two constants, T and μ, i.e., the temperature and the chemical potential. Finding the second constant μ is an important task for modern physics, because this constant represents the chemical potential of the Universe.

Spectral perturbations of a different kind, so-called y-distortions, are also of great interest. They arise at a much later epoch of the evolution, at $z \leqslant 10$, due to Compton scattering of photons by the hot plasma of galaxy clusters, and contain information about their structure, temperature, and the density of the intergalactic medium.

One planned project that could make a significant contribution to the study of CMB spectral features due to its sensitivity and high angular resolution is the Millimetron Space Observatory [22, 23]. Furthermore, currently proposed experiments, including lunar-based telescopes [7, 24–27], aim to study various types of CMB spectral distortions and would potentially provide crucial information about the physics of the early Universe, inaccessible to other observations.

Furthermore, it is worth noting that one specific type of CMB distortion is the anisotropic Sunyaev–Zel'dovich effect. Observation of this effect, analytically predicted in [28, 29], could help obtain independent estimates of the dipole, quadrupole, and octupole of the CMB anisotropy.

An additional and extremely important result of solving both problems, i.e., the study of CMB polarization and its frequency distortions, will include studying the emissions of dust and other foreground sources in the same frequency range.

2. Primary B-mode polarization

Linear polarization is a traceless second rank tensor, and, in general, in spherical coordinates, the Stokes parameters Q and U can be written as

$$\begin{aligned} Q(\mathbf{n}) + \mathrm{i}U(\mathbf{n}) &= -\sum_{\ell,m} (a^{\mathrm{E}}_{\ell,m} + \mathrm{i}a^{\mathrm{B}}_{\ell,m})\, {}_2Y_{\ell m}(\mathbf{n})\,, \\ Q(\mathbf{n}) - \mathrm{i}U(\mathbf{n}) &= -\sum_{\ell,m} (a^{\mathrm{E}}_{\ell,m} - \mathrm{i}a^{\mathrm{B}}_{\ell,m})\, {}_{-2}Y_{\ell m}(\mathbf{n})\,, \end{aligned} \tag{1}$$

where the unit-length vector $\mathbf{n}$ is expressed in terms of spherical coordinates $\mathbf{n} = (\theta, \varphi)$, and the functions ${}_{\pm 2}Y_{\ell m}(\mathbf{n})$ are spin-weighted spherical harmonics with spin ± 2. Thus, similarly to how a vector field can be separated into gradient and vortex components, the tensor polarization field is naturally separated into 'electric' E and 'magnetic' B components.

During the inflationary stage, both scalar and tensor perturbations are generated. Tensor perturbations of the metric are the source of the magnetic B-mode polarization of the CMB radiation. Thus, a reliable detection of the primordial B-mode would provide evidence for the inflation hypothesis. However, the problem lies in detecting the primordial cosmological B-mode, whose presence in the observed signal is obscured by polarized foregrounds (primarily due to dust emission from our Galaxy).

We note that, along with tensor perturbations generated during the inflationary stage, topological defects — primarily cosmic strings — are possible sources of the B-mode polarization of the CMB. Even more exotic mechanisms may also play a role [30–36]. Although, as shown by M Hindmarsh and other researchers, such alternatives cannot account for the generation of the entire B-mode polarization of the CMB, their contribution may be comparable by order of magnitude to that expected from gravitational waves of inflationary origin. Observational methods have not yet allowed completely ruling out this scenario, and it continues to be considered an important complement to the standard inflationary picture.

To extract the primordial mode, it is necessary to separate the useful signal from the foreground. The majority of these foreground signals can be separated using multifrequency observations. However, due to the weakness of the desired signal, uneliminated foregrounds typically persist, which

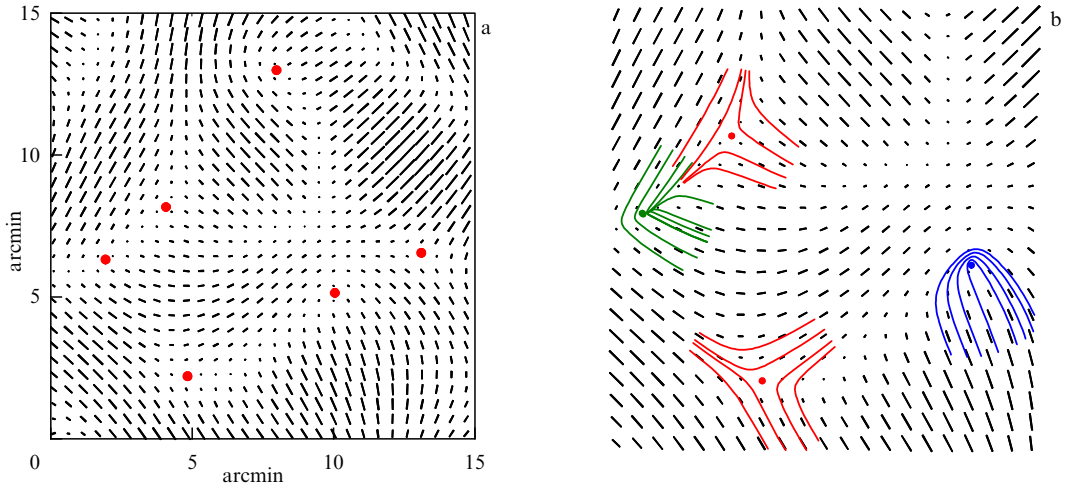

Figure 1. (a) CMB radiation polarization field. Lengths of segments are proportional to linear polarization $\sqrt{Q^2+U^2}$. Their directions correspond to polarization direction: $\tan(2\varphi) = U/Q$. Red dots are placed at locations where polarization vanishes. (b) Unpolarized dots of different types. Red denotes 'saddles,' blue denotes 'comets,' and green denotes 'beaks.' (From [39].)

must be separated using specific data processing methods and tested for Gaussianity. Although some inflationary models initially produce small deviations from Gaussianity [37, 38], such deviations are nonetheless significantly smaller than the non-Gaussian contribution of the foregrounds to the observed signal. Therefore, to isolate the signal generated by inflation, it should be assumed that this signal obeys Gaussian statistics.

2.1 Gaussianity test

Various methods are used to investigate the nature of the observed signal and determine whether it is Gaussian or non-Gaussian. Starting from the original papers [40, 41] (BBKS) and [42] (BE) on the statistics of random fields, highly effective approaches have been developed for scalar and tensor fields, such as Minkowski functionals [43–52], higher-order correlations [53–63], local extremum statistics [64, 65], peak clustering [66–69], Kullback–Leibler divergence [70], percolation [71], and the study of statistics using neural networks [72, 73].

One of the most sensitive tests for Gaussianity, as applied to the polarization of the CMB, turned out to be a method based on the study of the statistics of unpolarized points in the sky [45, 74, 75], i.e., points where linear polarization disappears completely and the Stokes parameters vanish: $Q = U = 0$ (Fig. 1). It was found that there are three types of such points ('saddles,' 'beaks,' and 'comets,' depending on the behavior of the polarization directions in their vicinity) and, with the Gaussian statistics, the ratio of the numbers of points of different types to the total number of unpolarized points is independent of the power spectrum. This information does not relate to the power spectrum and only indicates the phase distribution, i.e., the Gaussian or non-Gaussian nature of the signal.

At the same time, the total number of such points in the sky depends on the correlation scale. Therefore, when processing polarization maps, it is possible to vary the maximum number of the ${}_{\pm2}Y_{\ell m}$ harmonics with $\ell \leqslant \ell_{\max}$ used in constructing the map. This method allows investigating the nature of the signal at different angular scales. Indeed, with increasing $\ell_{\max}$, the correlation scale decreases, the pattern becomes increasingly fine-scaled, and, accordingly, the total number of unpolarized points increases. A detailed study of the Planck data revealed a strong non-Gaussianity of the extracted signal for both the E-mode and B-mode polarizations at virtually all angular scales [39]. This indicates that the signal under study contains a polarized non-Gaussian foreground that was not eliminated from the observational data, or the map is heavily distorted by gravitational lensing (Fig. 2).

2.2 Extracting Gaussian signal from observations

In addition to traditional methods of pre-separating signal components using multi-frequency maps and then testing the remaining blackbody signal for Gaussianity, sophisticated methods for further purification are necessary. One such method is extracting the Gaussian component of the signal [76]. This approach is based on the intrinsic nature of inflation, which generates Gaussian perturbations.

The observed map of the CMB anisotropy or polarization contains the cosmological Gaussian signal of interest $g(\mathbf{n})$ and foregrounds of various origins $f(\mathbf{n})$,

$$s(\mathbf{n}) = g(\mathbf{n}) + f(\mathbf{n})\,, \tag{2}$$

where s is the total observed signal. The signal s can be viewed as a scalar value T of the CMB temperature or as the Stokes parameters Q or U. Two-point correlations $x_r = s_1 s_2$ consist of a set of products of two observed signals $s_1 = s(\mathbf{n}_1)$ and $s_2 = s(\mathbf{n}_2)$, separated by a fixed angular distance r such that $\cos r = \mathbf{n}_1\mathbf{n}_2$. Therefore, we can write

$$x_r = s_1 s_2 = g_1 g_2 + g_1 f_2 + g_2 f_1 + f_1 f_2\,. \tag{3}$$

Only the first term on the right-hand side of this equation corresponds to Gaussian correlations. The distribution of $g_1 g_2$ can be found analytically [76]:

$$P_{gg}(x_r) = \frac{1}{16\pi\sqrt{1-\gamma^2}} \int_1^\infty \exp\left[-\frac{(t-\gamma)x_r}{4(1-\gamma^2)}\right] \frac{\mathrm{d}t}{\sqrt{t^2-1}}\,, \tag{4}$$

where $\gamma = \xi_r/\xi_0$ ù $\xi_r = \langle x_r \rangle$ (Fig. 3). To separate these correlations from the non-Gaussian foreground component, the blind internal linear combination (ILC) method can be

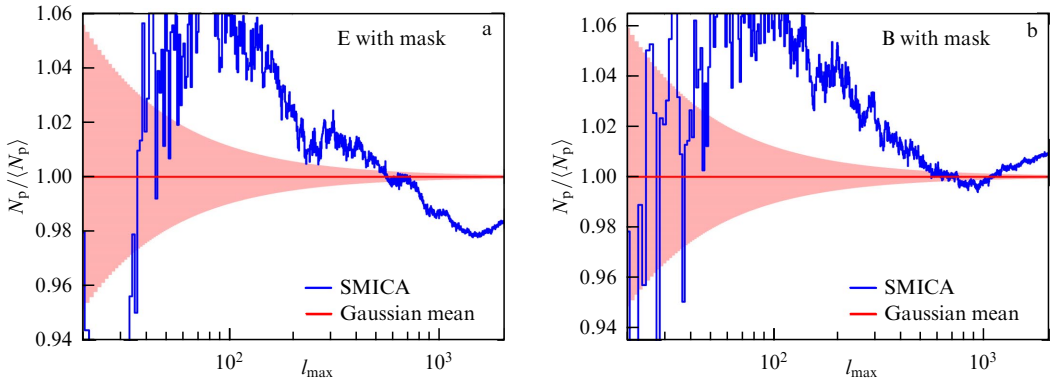

Figure 2. Number of unpolarized dots on celestial sphere as a function of number of harmonics used to construct map. Results are normalized to mean number of dots for Gaussian case. Red line shows expected mean number of dots for Gaussian field. Red zone shows 1σ deviation from mean. Blue color shows result of processing Planck (SMICA) data for (a) E- and (b) B-modes in presence of a mask obscuring Galaxy and some strong point-like foreground sources of polarization. (From [39].)

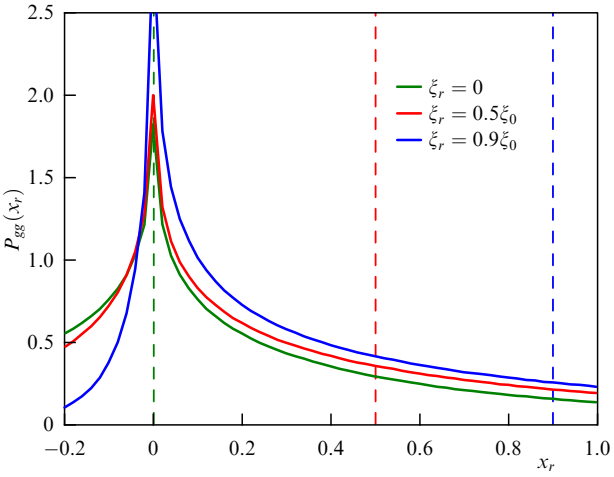

Figure 3. Distribution functions of two-point correlations $x_r = g_1 g_2$ for Gaussian signal g, normalized to unity at zero distance $r = 0$: $\langle x_0\rangle = 1$. Vertical lines show mean value, i.e., two-point correlation function $\langle x_r\rangle = \xi(r) = \int x_r P_{gg}(x_r)\,\mathrm{d}x_r$. (From [76].)

used [77]. With additional information on the spatial correlation of foregrounds (primarily dust), more effective methods can be applied, which will be discussed in Section 3 in connection with the problem of foreground separation in multi-frequency observations.

We note that the approach described above, unlike traditional methods, does not reproduce a map of the purified signal. This method reconstructs the purified two-point correlation function or the equivalent power spectrum of the Gaussian component of the signal, i.e., the signal generated during the inflationary stage.

3. Spectral distortions

As noted in the Introduction, one of the main goals of future experiments related to the study of the CMB is to observe its spectral distortions. Among the observed distortions associated with the nature of the CMB itself, one can distinguish μ-distortions I_μ, the Sunyaev–Zel'dovich thermal effect I_{y_0}, the first and second relativistic corrections to this effect I_{y_1} and I_{y_2}, and the CMB anisotropy I_{CMBA} (this type of spectral distortion is the temperature derivative of blackbody radiation). It is assumed that the CMB monopole can be easily subtracted from observational data. All these spectra have clearly defined shapes:

$$
\begin{aligned}
I_\mu(\nu) &= I_0\,\frac{x^4\exp x}{(\exp x-1)^2}\left(\frac{1}{b}-\frac{1}{x}\right)\mu\,,\\
I_{y_0}(\nu) &= I_0\,\frac{x^4\exp x}{(\exp x-1)^2}\left[x\coth\left(\frac{x}{2}\right)-4\right]y\,,\\
I_{y_1}(\nu) &= I_0\,\frac{x^4\exp x}{(\exp x-1)^2}\,Y_1(x)\theta_{\mathrm{e}}y\,,\\
I_{y_2}(\nu) &= I_0\,\frac{x^4\exp x}{(\exp x-1)^2}\,Y_2(x)\,\theta_{\mathrm{e}}^2 y\,,\\
I_{\mathrm{CMBA}}(\nu) &= \frac{2(k_{\mathrm{B}}T_0)^3}{(hc)^2}\,\frac{x^4}{(\exp x-1)^2}\,\frac{\Delta T}{T_0}\,,
\end{aligned}
\qquad (5)
$$

where $x = h\nu/k_{\mathrm{B}}T_{\mathrm{CMB}}$, the CMB monopole temperature is $T_{\mathrm{CMB}} = 2.72548$ K [20, 21], and $\Delta T/T_{\mathrm{CMB}} < 10^{-4}$. The same estimated values for the constants b, I_0, μ, and y are used as in [25]: $I_0 = 270$ MJy sr^{-1}, $b = 2.1923$, $\mu = 2\times10^{-8}$, $y = 1.77\times10^{-6}$, and $\theta_{\mathrm{e}} = k_{\mathrm{B}}T_{\mathrm{SZ}}/m_{\mathrm{e}}c^2 \sim 2.44\times10^{-3}$. The functions $Y_1(x)$ and $Y_2(x)$ for the first and second corrections are rather cumbersome; analytical formulas for them can be found in [78]. The θ_{e} value is treated here as the sky-average one. For individual galaxy clusters, it is, of course, significantly larger.

3.1 Separating signal components

To successfully distinguish different types of spectral distortions, they must be separated, first, from each other, and second, from foregrounds of cosmic and instrumental origin. These foregrounds are discussed in detail in Sections 3.2 and 4. They include dust emission, synchrotron radiation, cosmic infrared background (CIB), free–free emission, CO lines, and radiation from telescope optics.

When experimental sensitivity is limited, it is necessary to use appropriate, effective methods for separating signal components. The main problem lies not only in the small magnitude of a given spectral distortion but also in the lack of information about the spectral shape of the foregrounds. In such cases, given a known spectral shape of the signal, the ILC method is often successfully applied. Its drawback is that the combination of different foregrounds can, to a certain extent, mimic the desired signal. Therefore, it has been modified by

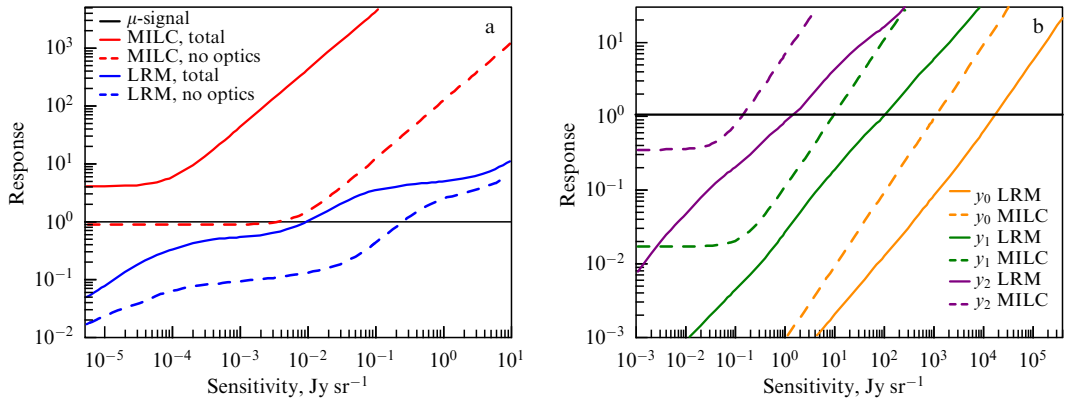

Figure 4. Estimation of required sensitivity and comparison of MILC and LRM methods. (a) Total response of linear data processing method (MILC or LRM) to photon noise (all foregrounds, including optical system of telescope), compared with unit response to μ-signal as a function of photon noise (or sensitivity of experiment). Intersection with horizontal line effectively provides estimate of required sensitivity for measuring monopole part of μ-perturbation (chemical potential of Universe). Dashed lines show responses to foreground + noise without taking telescope's optical system into account. This demonstrates that foreground created by optical system greatly complicates the problem. (b) Response to foregrounds and noise in the case of y-perturbation measurements. Calculations were performed for 384 frequency channels covering range from 15 GHz to 4 THz. (From [79].)

the constrained ILC (cILC) [80–82] and moments ILC (MILC) [83–85] methods, which guarantee the exclusion of the response to certain specific spectra from the final result. However, with a large number of foreground signals that need to be eliminated, the number of additional conditions imposed can become excessive and naturally lead to a strong response to random photon noise. To mitigate this effect, the least-response method (LRM) [79] (Fig. 4) was developed. It ensures a minimal response to all foregrounds with poorly defined parameters and to photon noise, while maintaining a single response to the signal of interest.

3.2 Optimal temperature of optical system

The optical system of a telescope has its own unique characteristics, namely, absorption capacity and temperature. Furthermore, different optical components (mirror panels, reflecting mirrors, gaps between panels) can have their own temperature characteristics, which change during a mission. The orientation of the primary mirror relative to the Sun also affects the temperature regime. The characteristics of the cooling system are typically such that they cannot ensure a completely uniform temperature for all components of the reflective surface during observations.

Thus, the optical system creates two main interferences to observations: photon noise and a foreground signal, which changes over time. When studying the local Sunyaev–Zel'dovich effect and its corrections, it is possible to conduct simultaneous measurements of signals from two points in the sky. The difference between these signals eliminates the foreground created by the optics. A different situation arises when measuring a monopole μ-signal. In this case, the spectral channels must be calibrated for blackbody radiation, and the foreground created by the optical system must be taken into account when processing the observations. The LRM can be used to handle this task if the optical-system temperature is properly selected. Importantly, the optical system must not be overcooled. The lower the mirror temperature, the lower the photon noise it produces, which increases the sensitivity of the experiment. However, as the optical-system temperature approaches 2.73 K, i.e., the CMB temperature, the foreground created by the mirror begins to mimic spectral distortions due to temperature deviations of its different parts from the average.

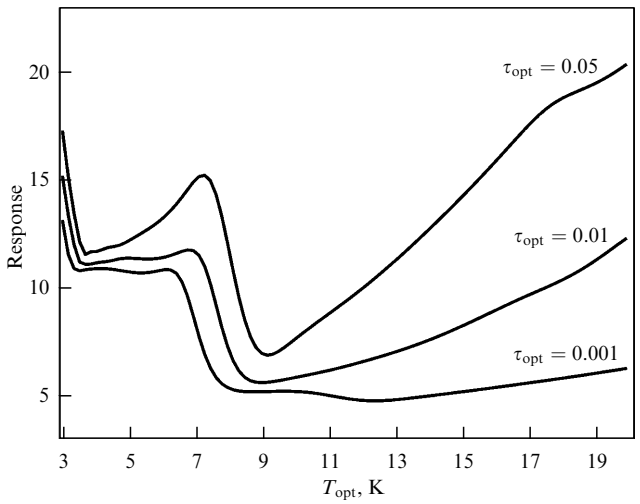

Figure 5. Total response to all foreground and noise as a function of average temperature of telescope optical system at sensitivity of 1 Jy sr^{-1} for different values of its surface emissivity τ. Minimum response is attained at temperature $T_{opt} \sim 9$ K. (From [79].)

Figure 5 shows the dependence of the response to cosmic foregrounds and the foreground created by the optical system on its temperature for different emissivity values. At temperatures close to T_{CMB}, this response increases explosively. At higher temperatures, however, the response increases due to an increase in photon noise. The optimal temperature for measuring μ-distortions is $T \sim 9$ K [79].

4. Foreground radiation problem

In addition to CMB photons, the Universe contains a large number of photons created during the evolution of galaxies, which pose a significant challenge to the search for weak signals of cosmological origin. In this section, we summarize current knowledge about the spatial and frequency structure of these foregrounds, which can be used to eliminate them from observational results.

An important characteristic of many foregrounds is their spatial fluctuations. First, the foreground is weaker in some parts of the sky than in others, allowing the most suitable

areas to be selected for CMB observations. Second, information about spatial fluctuations can be used to separate the foreground from the signal, which is uniformly distributed across the sky. For example, when searching for spectral distortions using the Millimetron Observatory, it is necessary to know how the foreground fluctuates on the spatial scales accessible to this telescope in single-dish mode: from 6 arcseconds (corresponding to an angular resolution at 1 THz) to a few degrees (the estimated maximum field of view is several square degrees).

Because the Millimetron Observatory will have a unique angular resolution unattained by previous observatories in some spectral ranges, sufficiently detailed sky maps with the required resolution do not exist for many types of foregrounds. To compensate for this deficiency, it is necessary to add random small-scale foreground fluctuations, which is easy to do if their spatial spectrum is known. This will allow obtaining maps with the Millimetron resolution for all foreground sources.

The traditional HEALPix sky pixelization [86] is used to construct and analyze foreground emission maps. For example, observation results of the Planck space observatory are available in this pixelization.

4.1 Generating small-scale intensity maps

As noted above, the angular resolution of the available data may be insufficient to model the sky for the Millimetron Observatory. For example, the angular resolution of the Planck Observatory is approximately seven times worse than that of the Millimetron Observatory. In the final products provided by the Planck team, the pixel size is 1.9×1.9 arcminutes, which is 20 times larger than the required 6 arcseconds. Therefore, the missing small-scale information is added artificially. This is easily done for foregrounds that are accurate realizations of a Gaussian random process, such as the anisotropy of the CMB, which is considered Gaussian [87]. Such processes are fully characterized by their power spectrum. For the CMB temperature anisotropy, the shape of the power spectrum is well known and can be modeled at all required scales using the CLASS code [88].

To construct a random realization of a correlated two-dimensional Gaussian field (e.g., the CMB temperature anisotropy), we invoke a method well known in the literature, which is used to create initial conditions for cosmological simulations [89]. In this approach, an uncorrelated random field (white noise) $F_{\rm W}$ with zero mean and unit amplitude is first generated. It is then convoluted with a transfer function corresponding to the specified power spectrum. This produces the random field $F_{\rm R}$.

Now, we need to combine the resulting random field with the observed $F_{\rm O}$ realization. For this, the observed realization is convoluted, for example, with a Gaussian kernel with a width corresponding to the Planck Observatory resolution, and the random field is convoluted with a complementary kernel that cuts off low-frequency harmonics from $F_{\rm R}$. The convolution results are added together to produce the desired map.

The described map-generation algorithm can be conveniently written for the Fourier transforms of maps. We obtain a random realization of a two-dimensional Gaussian process with a given power spectrum,

$$\tilde{F}_{\rm R} = \tilde{F}_{\rm W}\sqrt{P(k)}\,, \tag{6}$$

where $\tilde{F}_{\rm R}$ and $\tilde{F}_{\rm W}$ are discrete Fourier transforms of the maps of the desired random field and white noise, and $P(k)$ is the power spectrum of the generated field, calculated for all discrete frequencies k. For the resulting map,

$$\tilde{F}_{\rm G} = \tilde{F}_{\rm O}\,G + \tilde{F}_{\rm R}(1-G)\,, \quad G = \exp\left(-\frac{k^2}{2\sigma^2}\right). \tag{7}$$

This approach can also be used for maps of galactic dust parameters and of synchrotron radiation, but not of the extragalactic foreground. The formation of the last is associated with the nonlinear stage of growth of the large-scale structure of the Universe, and therefore the foreground is not described by a Gaussian process.

4.2 Cosmic microwave background anisotropy

The most powerful background radiation at wavelengths of about 1 mm is the CMB. It is approximately thermal and nearly isotropic radiation with a temperature of 2.73 K. There are also small-scale fluctuations in the CMB temperature (cosmological anisotropy) with an amplitude of about 10^{-5}, caused by the inhomogeneity of the Universe. The temperature, and therefore the intensity, of the CMB is distributed primarily across the sky as a dipole with an amplitude of about 10^{-3} (caused by the observer's motion relative to the preferred reference frame in which the CMB is at rest). This dipole component is completely removed from the CMB maps by subtracting the $\ell = 1, m = -1, 0, 1$ spherical harmonic coefficients from the anisotropy data. We also note that the cosmological dipole can be separated from the effect associated with the observer's motion relative to the CMB by measuring the anisotropic Sunyaev–Zel'dovich effect from nearby galaxy clusters [28, 29].

We use the CMB and foreground maps obtained by the Planck Space Observatory and presented in the third data release [90]. These maps were obtained by processing the raw data, which included converting the data to HEALPix pixelization, removing noise, and separating the intensity maps into several diffuse components: CMB, galactic dust emission, synchrotron emission, free–free emission, and the extragalactic foreground. Furthermore, a significant processing step is the removal of the contribution of bright extragalactic sources, which represent unresolved sources in the intensity and polarization maps. To eliminate such objects, special masks based on the Planck catalogs [91] are used (the standard point source mask COM_Mask_PointSrc, COM_Mask_GalPlane for cutting out the galactic plane, and the polarization confidence mask). Their use is especially important when analyzing polarization fluctuations and statistics (including the B-mode), because even a single bright source can distort the spectra and introduce non-Gaussian artifacts. Paper [92] is devoted to the separation of components. Several methods were used for this separation: COMMANDER, NILC, SEVEM, and SMICA. Component maps have been published for all of these methods. These methods yield results that are largely consistent within their error bars. That is why the maps obtained by the COMMANDER method were used in subsequent work. The maps themselves can be obtained from the Planck Observatory [1] archive webpage, where the data presentation format is also described.

[1] https://wiki.cosmos.esa.int/planck-legacy-archive/index.php/CMB_maps.

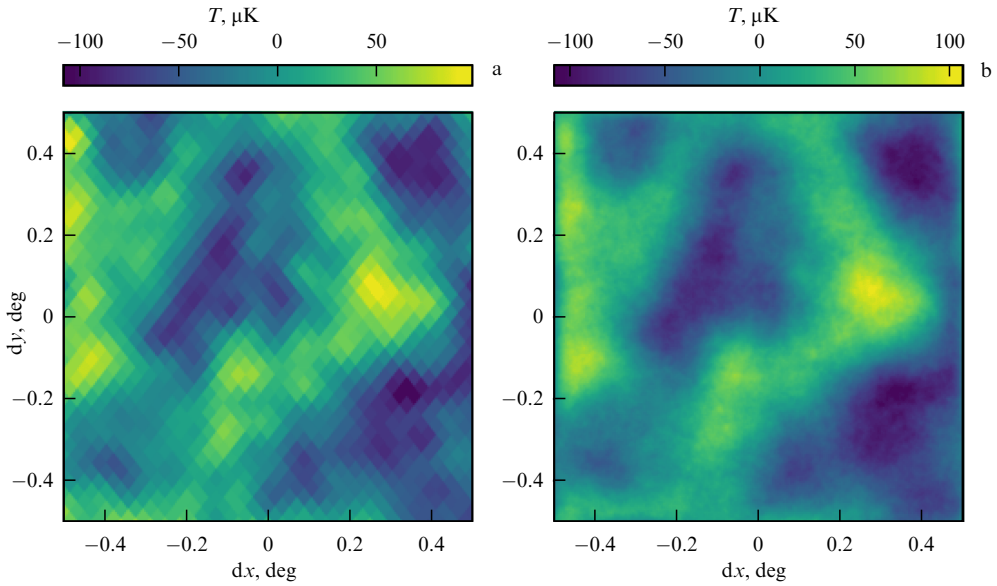

Figure 6. Map of CMB temperature anisotropy in 1 × 1-degree field centered on a point with galactic longitude 45° and galactic latitude 80°. (a) Original Planck map; individual pixels are visible. (b) Planck map supplemented with generated small-scale anisotropy.

Figure 6 shows an example of a CMB anisotropy map over a 1 × 1-degree region near the galactic north pole. Both the original map based on Planck data and a map supplemented with random small-scale perturbations are shown. Silk damping causes the CMB anisotropy power spectrum decrease on small angular scales. Upon comparison of Figs 6a and 6b, the added small-scale perturbations do not significantly change the distribution of dark and light spots corresponding to positive and negative deviations in the CMB temperature. However, Fig. 6b does show features smaller than the pixels in Fig. 6a.

4.3 Galactic dust emission

Another key foreground source is the thermal emission from galactic dust. The dust emission spectrum is quite complex [93], but its shape can often be described using a gray body model with spectral slope β [94],

$$I(\nu) = \tau \frac{2h\nu^3}{c^2\left[\exp\left(h\nu/(k_B T)\right) - 1\right]} \left(\frac{h\nu}{k_B T}\right)^{\beta}, \qquad (8)$$

where τ is the dust emissivity.

The Planck team used spectrum shape (8), and therefore maps of the distribution of τ, T, and β across the sky are available in their data archive. The Planck collaboration recommends using maps obtained from 2015 rather than 2018 data, because the latter, due to a different approach to raw data analysis, resulted in insufficient CO lines subtraction, which impacted the quality of the reconstruction of dust thermal emission parameters. Figure 7 shows the dust emissivity distribution τ. It is clear that the greatest amount of dust is observed in the galactic plane.

For the Millimetron project, dust parameter maps can be modeled at the required resolution using the same approach as for the CMB temperature anisotropy, namely, using Planck data on scales greater than 2 arcminutes and supplementing them with synthetic data on smaller scales. This was done using measured dust power spectra in the scale range from 1 degree to 2 arcminutes, which were approximated by power-law functions and extended to a scale of

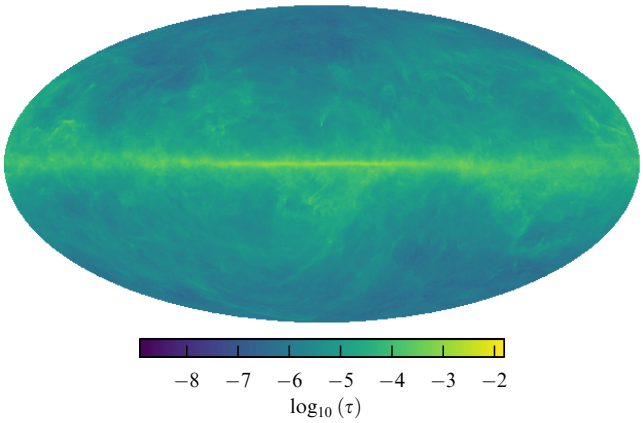

Figure 7. Distribution of dust emissivity τ on celestial sphere according to Planck data.

6 arcseconds. The resulting dust parameter maps are presented in Fig. 8. As can be seen from Fig. 8, the emissivity of dust undergoes the strongest small-scale variations. The spectral slope parameter β changes only on large scales, because the Planck Observatory data do not allow this parameter to be accurately measured on small angular scales [95].

4.4 Synchrotron radiation

The intensity and spectrum of synchrotron radiation depend on the magnetic field strength and the energy distribution of relativistic particles along the line of sight. The synchrotron radiation spectrum can be described over a wide frequency range by a power function with an exponent that varies smoothly with frequency [96],

$$I_s = A_s \left(\frac{\nu}{\nu_s}\right)^{\beta_s + c_s \log(\nu/\nu_s)}, \qquad (9)$$

where $\nu_s = 30$ GHz is the characteristic frequency, A_s is the amplitude, β_s is the slope of the spectrum at the characteristic frequency, and c_s is the rate of change of the slope with frequency.

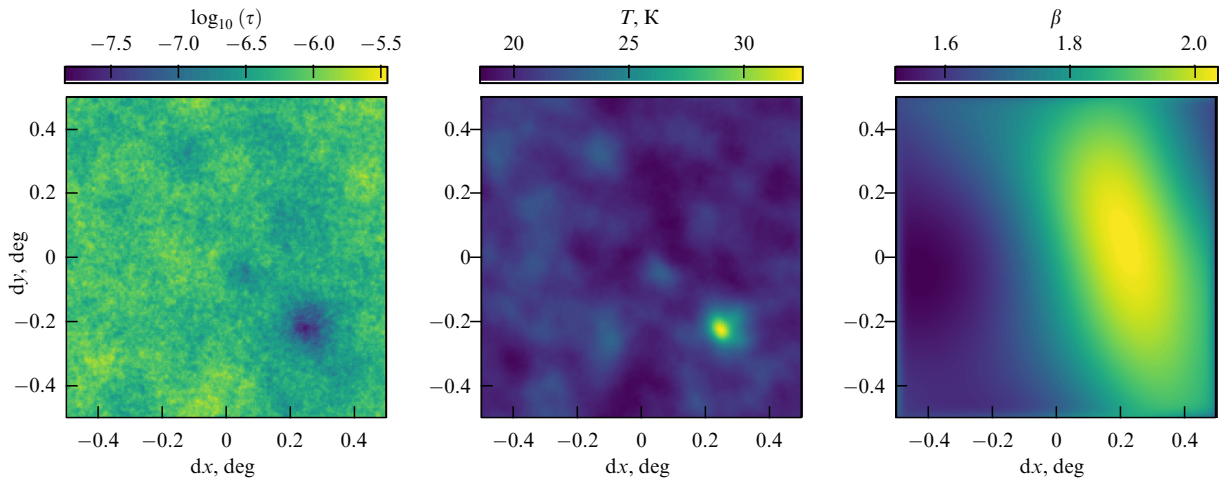

Figure 8. Maps of distribution of three dust parameters for emission model (8) in 1 × 1-degree field centered on a point with galactic longitude 45° and galactic latitude 80°.

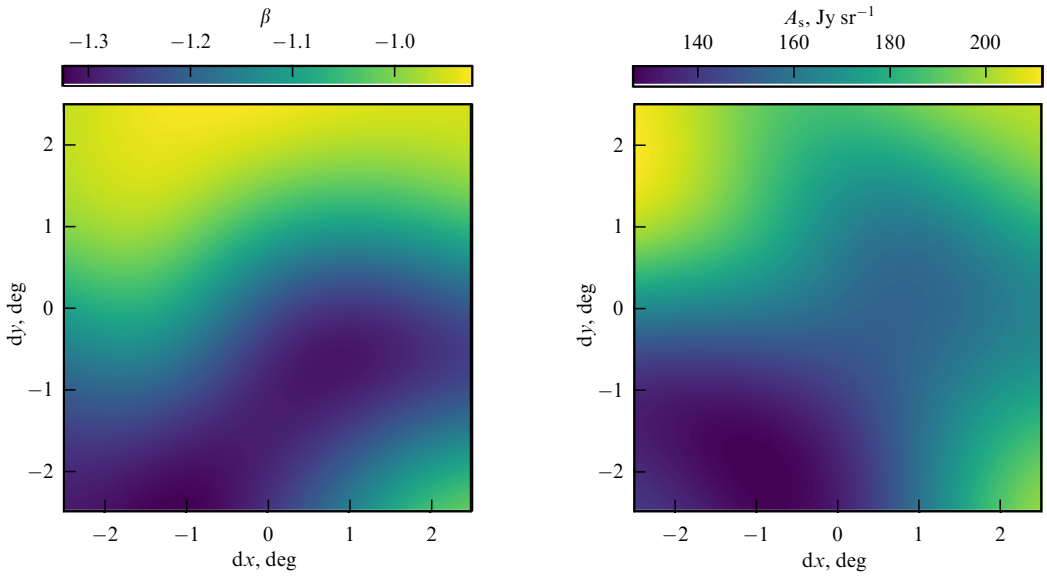

Figure 9. Spectral slope and amplitude of synchrotron radiation in 5 × 5-degree field centered on a point with galactic longitude 45° and galactic latitude 80°.

The parameters A_s, β_s, and c_s vary across the sky, but the spectral coverage of the Planck Observatory's receivers is already insufficient to measure spectral index variations [95]. Therefore, the Planck collaboration decided to fix the spectral index, and their data archive contains only synchrotron emission amplitude maps. In the case of the WMAP Observatory [97], the sky was divided into 12 regions with different spectral indices.

The most detailed information on synchrotron emission spectrum variations across the sky can be obtained from the results of the ground-based S-PASS [98] and QUIJOTE [96] projects, which conducted measurements at frequencies of 2–40 GHz, and supplementing these data with the WMAP and Planck results. They showed significant variations in the spectral index in different parts of the sky. According to their results, β_s ranges from −1.4 to −0.3,[2] and c_s, from −0.4 to 0.4.

[2] Here, it is assumed that I_s in (9) is expressed in units of intensity, Jy sr^{-1}. If I_s is expressed in units of temperature, it is necessary to subtract 2 from β_s.

The SPASS and QUIJOTE results were obtained for more than half of the sky, including low galactic latitudes. Near the galactic poles, the ranges of β_s and c_s can be smaller, according to the results in [96], but the largest possible ranges are used to estimate the influence of the foreground when searching for weak spectral distortions in the CMB.

Maps of synchrotron spectrum parameters based on the QUIJOTE project results (version 1) can be downloaded from the project archive website, https://lambda.gsfc.nasa.gov/product/quijote/quijote_mfi_data_get.html. These maps have low resolution, with a pixel size of approximately 1 degree. Because variations in the synchrotron radiation spectrum have not been studied at small scales, we do not supplement these data with random small-scale perturbations; rather, we smooth them, i.e., interpolate. Example maps for synchrotron radiation parameters are shown in Fig. 9.

4.5 Free–free emission

Another component of the galactic foreground is the free–free emission of ionized hydrogen. To describe the frequency spectrum of this component, the Planck collaboration

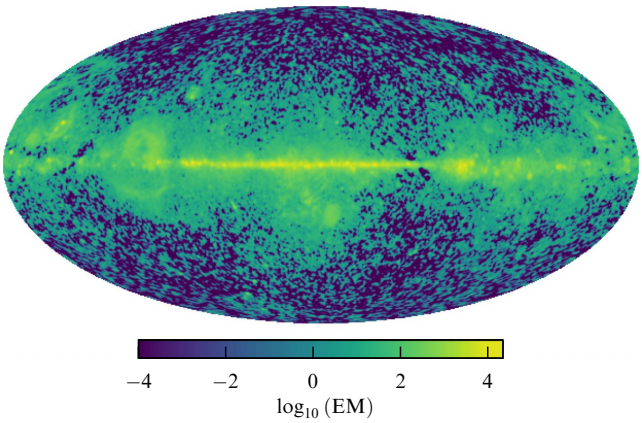

Figure 10. Map of emission measure of free–free gas transitions in Galaxy based on Planck data.

adopted the formula [95]

$$I_{ff} = 3.51 \times 10^{-14} T_{\rm e} \left(1 - \exp\left(-\tau\right)\right) \nu^2 \ \ [\text{Jy sr}^{-1}]\,, \qquad (10)$$

$$\tau = 0.05468\, T_{\rm e}^{-3/2} \nu_9^{-2}\, \text{EM}\, g_{ff}\,, \qquad (11)$$

$$g_{ff} = \log\left\{\exp\left[5.960 - \sqrt{3}/\pi \log\left(\nu_9 T_4^{-3/2}\right)\right] + \text{e}\right\}, \qquad (12)$$

where $T_{\rm e}$ is the electron temperature, τ is the optical depth, and EM is the emission measure. For brevity, we also use the notations $T_4 = T_{\rm e}/10^4$ and $\nu_9 = \nu/10^9$. In the data provided by the Planck collaboration, the electron temperature $T_{\rm e}$ ranges within 6990–7010 K. Consequently, the spectrum of this background experiences virtually no fluctuations in the sky; only its intensity, determined by the emission measure, varies. The emission measure distribution map is shown in Fig. 10.

4.6 Continuum emission from distant galaxies

Other galaxies, like our own, also emit far-infrared radiation due to dust present in the interstellar medium [99]. However, due to their remoteness, each galaxy emits only within a small region of the celestial sphere. Galaxies exhibit maximum far-infrared luminosity during the so-called cosmic noon, when the Universe is 1.5–7 billion years old [100–103]. During this era, galaxies experienced their most powerful bursts of star formation, accompanied by the production of large quantities of dust, which absorbed and re-emitted a significant portion of starlight, leading to the formation of the cosmic infrared background (CIB) [104, 105]. Because such galaxies have redshifts $z = 1$–3, the currently observed foreground spectrum has a peak at a wavelength of about 200 μm or a frequency of 1.5 THz, but, for measurements of the CMB spectrum, this foreground must also be taken into account at lower frequencies starting from 30 GHz.

The CIB spatial distribution corresponds to the distribution of galaxies in the sky, but when conducting observations with single telescopes in the far-IR range, one significant nuance becomes important: the angular resolution of even a 10-meter telescope at a wavelength of 200 μm is insufficient to resolve individual galaxies, because the average angular separation between galaxies is smaller than the diffraction limit of such a telescope. This leads to a confusion problem: the inability to separate the image of a point source from the background, because the background itself consists of similar overlapping images [106]. An example of a region of the sky with an infrared background, as seen by Millimetron, is shown in Fig. 11, which presents a simulated false-color image obtained in [107].

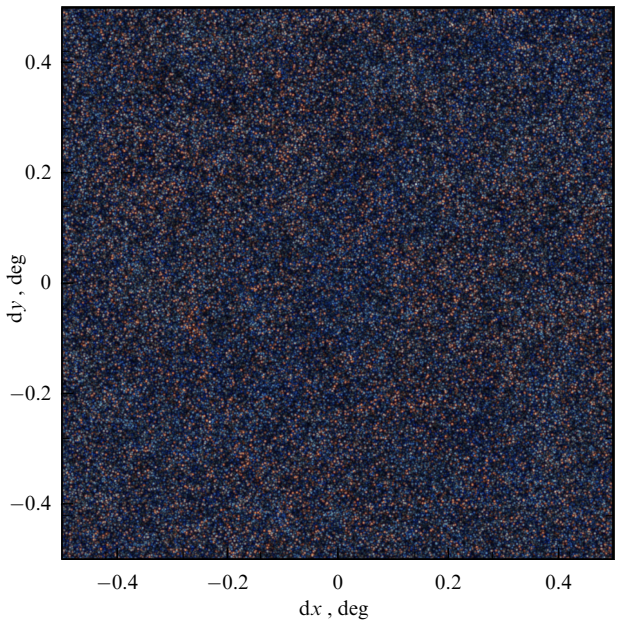

Figure 11. Map of IR background intensity distribution created by distant galaxies from model in [107], in artificial colors at frequencies of 300 GHz (red), 1 THz (green), and 3 THz (blue).

The Planck and Herschel observatories obtained infrared background maps with a resolution corresponding to the angular resolution of these observatories. Because the resolution in both cases is significantly worse than that of the Millimetron Observatory, and the observed foreground fluctuations are highly resolution-dependent, modeling is necessary. The model in [107] and its subsequent improvements [108, 109] are based on cosmological numerical models of the evolution of the large-scale structure of the Universe. The dark matter clumps formed in these models — halos — are assigned luminosities and infrared emission spectra according to specific recipes to match the diverse available observational data. In particular, these models reproduce the integrated background spectrum, source counts in different ranges, and the angular power spectrum of background intensity fluctuations.

Figure 12 shows another way to represent this background: this is what the CIB spectra would look like in randomly selected directions when observed with the Millimetron Observatory. Each spectrum is a combination of the spectra of individual galaxies with different intensities and different redshifts, which makes the shape of these spectra complex.

It is evident that the spectra in each pixel differ significantly from the average spectrum and from each other. The difference is greatest at high frequencies and decreases toward low frequencies. Nevertheless, these spectra represent some combination of gray bodies, and hence filtering methods capable of removing the contribution of gray bodies with characteristic temperatures of 10 to 30 K will undoubtedly be able to separate the useful signal from the continuum portion of the extragalactic IR background.

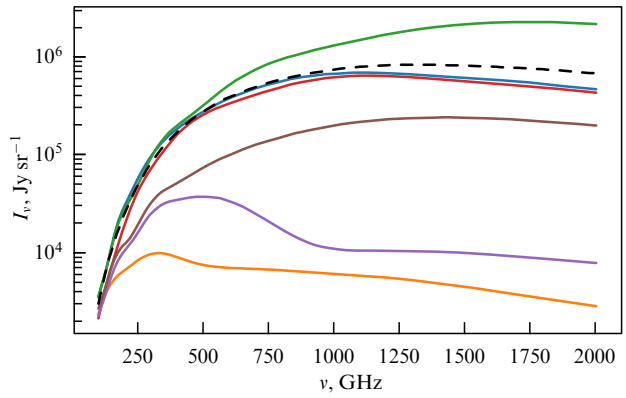

Figure 12. Examples of extragalactic IR background spectra created by distant galaxies in different directions within region measuring 1×1 degree (solid lines). Dashed line shows average extragalactic foreground spectrum.

4.7 Emission from distant galaxies in spectral lines

As shown in [110], approximately 1% of the entire IR background created by distant galaxies is made up of emission from these galaxies in spectral lines, primarily rotational transitions of CO molecules. The foreground intensity in CO lines must therefore be 10^2–10^4 Jy sr^{-1}, which is significantly higher than the intensity of the sought CMB spectral distortion signal. Unlike the continuum emission from galaxies, spectral lines appear at random locations in the spectrum, and hence the contribution of individual lines cannot be eliminated using linear filtering methods. For this reason, spectral lines pose a significant challenge for CMB spectrum measurements. Two approaches can help address this: selecting regions of the sky that are as free of galaxies as possible and averaging over these regions, resulting in a relatively smooth foreground that can then be filtered out. A comprehensive study of these approaches has not yet been conducted, and we present here only simple estimates based on literature data.

Figure 13a shows the spectrum of a typical galaxy where stars are being actively formed. Figure 13b shows data obtained by the ALMA observatory: CO molecule lines belonging to various galaxies detected in a region approximately 1 arcminute in size [111]. When observed with a spectrometer with a 15-GHz bandwidth, these lines contribute to the foreground intensity, shown by the blue stepped line.

The rotational spectrum of the CO molecule is a set of lines with frequencies that are multiples of 115 GHz. The lowest-frequency line, 115 GHz, corresponds to the transition from the first excited rotational state to the ground state and is denoted as CO(1-0). The next line, CO(2-1), has a frequency of 230 GHz, and so on. Because the quadrupole emission is strongly suppressed compared to the dipole emission, only transitions in which the rotational quantum number J changes by 1 are important. Sometimes, instead of specifying the initial and final quantum numbers (e.g., 1-0), only the upper number is specified (e.g., $J_{\rm up} = 1$).

The observation of CO lines is an important tool for studying galaxies. The luminosity in lines with a low rotational quantum number $J_{\rm up} \leqslant 4$ is practically independent of the physical state of the molecular gas and is determined only by its mass. Lines corresponding to higher excited levels arise in a medium with a sufficiently high temperature and density and are indicators of active star formation and core activity, and are a consequence of the propagation of shock waves in the interstellar medium (see, e.g., [113]).

Astrophysicists have long been developing models for calculating the emission of galaxies in CO lines. A numerical code for calculating the thermal and chemical equilibrium state of a gas cloud with given parameters (size, density, and metallicity) was used in [114]. The parameters of the Orion Nebula were used as the starting set of parameters. It is assumed that the simulated galaxy contains 3×10^5 clouds, similarly to the Orion Nebula. A model spectrum of the galaxy was obtained, and conclusions were drawn about the possibility of observing such objects even at high redshifts.

In [115], a numerical hydrodynamic cosmological model was used to calculate the formation and evolution of an individual galaxy. The radiative cooling of gas via atomic emission lines, star formation, and the influx of energy from stars and supernovae into the interstellar medium were taken into account in the model. Next, based on known correlations between molecular hydrogen production and the metallicity and pressure of the medium, a three-dimensional model of the distribution of molecular hydrogen in the galaxy at a redshift of $z = 3.5$ was constructed. A fixed ratio between the amounts of molecular hydrogen and carbon monoxide was used. Using Goldreich and Kwan's model [116], the population levels of CO molecules were calculated, resulting in model maps of the galaxy's CO emission. The brightness ratios of the various CO lines in the integrated spectrum of the galaxy were found to be within the scatter of similar ratios in observed galaxies.

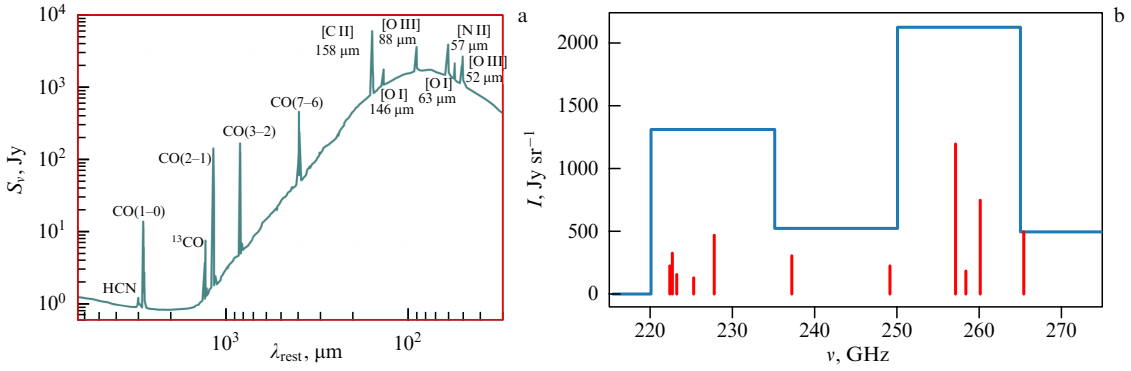

Figure 13. (a) Spectrum of nearby star-forming galaxy M82 from [112]. (b) Spectral lines of CO detected by APECS survey [111] (vertical lines) and estimate of their contribution to sky foreground intensity using 15-GHz-wide spectral channels (steps).

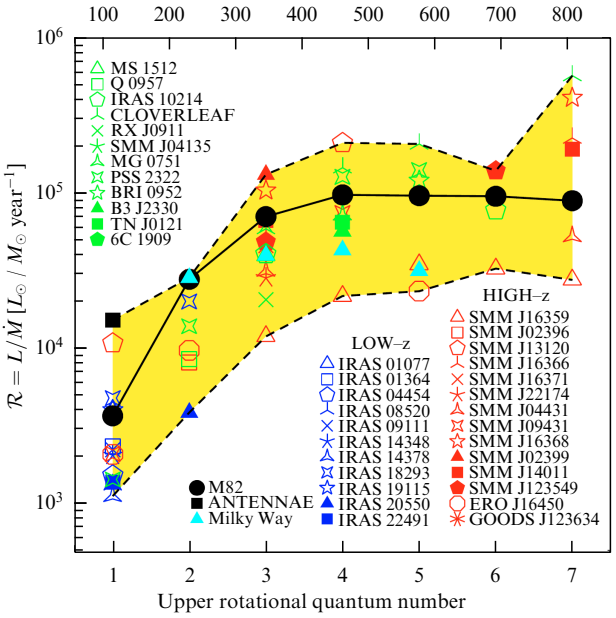

Figure 14. Ratio $\mathcal{R}$ of CO line luminosity to star formation rate as function of upper rotational quantum number for transitions in CO molecule [117]. Symbols show observational results; yellow area is characteristic range of $\mathcal{R}$ values for each line. Upper scale shows transition frequency in GHz.

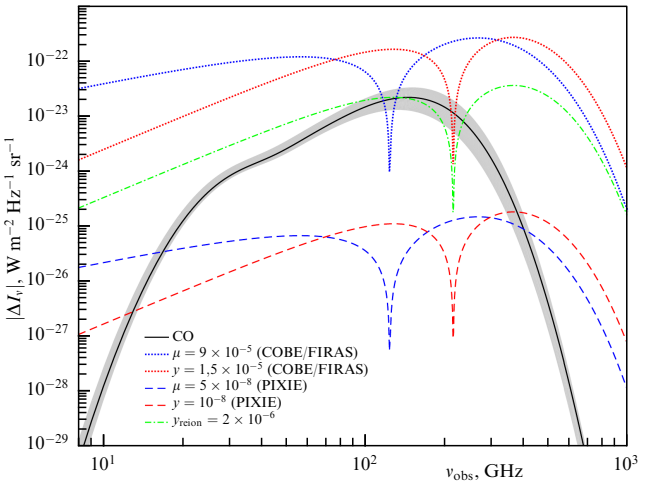

Figure 15. Sky-averaged spectrum of foreground created by CO lines in distant galaxies, according to model in [120]. For comparison, bounds for μ- and y-distortions of CMB spectrum from COBE/FIRAS data (dashed lines) and expected accuracy of PIXIE (dashed lines) are shown.

The two papers cited above demonstrate some success in creating models, but are not suitable for our estimates, because they model isolated objects. A method more suitable for this problem is proposed in [117]. First, using a well-known approach [118], typical histories of the mass growth of gravitationally bound objects in the Universe (halos) are calculated as a function of the redshift. It is then assumed that the mass growth rate is proportional to the star formation rate, which in turn is proportional to the CO line luminosity. This assumption is tested by analyzing galaxy observations; the result is shown in Fig. 14.

In [117], the integrated spectrum of CO line emission from distant galaxies was also obtained, along with line source counts and the angular power spectrum of the foreground intensity fluctuations created by these lines.

In [119, 120], the integrated spectrum of the foreground created by CO lines from distant galaxies was modeled to determine the possible influence of such a foreground on future measurements of CMB spectral distortions. For this purpose, the emission of individual molecular gas clouds with various parameters was modeled using the method of Goldreich and Kwan [116], and then a model dependence of the CO line luminosity on the star formation rate was constructed. Using a technique for comparing source counts in observations and cosmological numerical models, a dependence of the star formation rate on the galaxy mass was constructed, allowing the theoretically derived galaxy mass function to be converted into an integrated luminosity in CO lines. The authors concluded that the foreground created by CO lines has a significant amplitude (Fig. 15).

In [121], the possibility of separating the foreground spectrum obtained in [120] from the CMB μ-distortion signal was investigated. However, because the PIXIE instrument, for which the estimates in [120, 121] were performed, has extremely low angular resolution, the authors considered only the integrated foreground and did not examine regions of the sky with minimal foreground.

The results in [117] were significantly refined in [122], where, based on observations of a large number of galaxies for each CO line before the CO(13-12) transition, correlations were constructed between the line luminosity and the luminosity L_{FIR} in the far-IR range from 50 to 300 μm,

$$\log L_{\text{FIR}} = \alpha \log L'_{\text{CO}} + \beta\,, \tag{13}$$

where L'_{CO} is the CO line luminosity in units of K km s^{-1} pc^2, which is related to the luminosity in solar units by the relation

$$L'_{\text{CO}} = 3.8 \times 10^{-11} L_\odot \left(\frac{\nu}{\text{GHz}}\right)^3 \frac{L_{\text{CO}}}{\text{K km s}^{-1}\,\text{pc}^2}\,. \tag{14}$$

In [122], for each spectral line, the α and β parameters are given for the power-law function approximating the relation between the line and continuum luminosities, as well as the scatter s of the luminosities relative to this approximation. We applied the results in [122] to our model of submillimeter galaxies [107]. The CO lines were assigned a uniform width of 300 km s^{-1}. The result was a model data cube for the foreground created by the CO lines.

Example spectra are shown in Fig. 16. Obviously, due to the randomness of the foreground in each individual direction, linear filtering methods cannot eliminate this foreground for every observation direction. However, as can be seen from the dashed line in Fig. 16, averaging over a region of the sky significantly smoothes the spectrum. Thus, for an area 1×1 degree in size in the most important frequency range 100–300 GHz, the CO line foreground fluctuations no longer exceed 10 Jy sr^{-1}.

The spatial inhomogeneity of the CO line foreground, demonstrated in Fig. 17, can also be exploited. If all peaks brighter than 100 Jy sr^{-1} are eliminated from the foreground maps, the map averaged over the remaining pixels demonstrates a foreground level significantly lower than the average, shown by the green dashed–dotted line in Fig. 16. Another method for combating spectral line interference could be to increase the spectral resolution, which would allow the identification of individual bright lines that contribute most to the foreground.

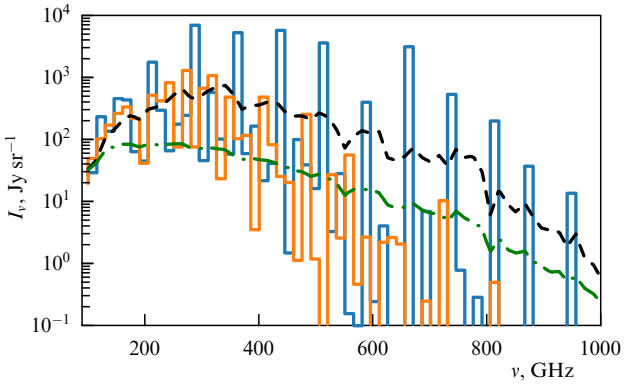

Figure 16. Examples of spectra of foreground created by CO lines from distant galaxies. Solid stepped lines show spectra that will be visible in two different directions by Millimetron Observatory. Dashed line shows spectrum averaged over 1×1-degree region of sky. Dashed-dotted line shows spectrum after removing all spots brighter than 100 Jy sr^{-1}.

4.8 Selecting optimal site for search for spectral distortions of cosmic microwave background

The sky foreground model we developed allows constructing radiation intensity maps in the 30–2000 GHz wavelength range for sky regions up to 1×1 degree in size. For the following sky foreground components, available observational data are used: CMB, galactic dust emission, synchrotron emission, and free–free emission. For the extragalactic foreground, the maps are completely random and are not therefore used to determine the most suitable sites.

Based on the expected capabilities of the Millimetron Observatory, as well as the above-identified features of the foreground created by CO lines from distant galaxies, it follows that the minimum site size for studying the CMB frequency spectrum is 1×1 degree. Model maps of this size were obtained for sky regions with galactic latitudes greater than 30 degrees (in absolute value) to eliminate the main contribution of galactic foregrounds. Map centers were chosen as pixel centers using the HEALPix scheme with $N_{\rm side} = 128$, which corresponds to a step (the distance between the centers of the nearest pixels) of approximately 0.5 degrees. This choice ensures complete coverage of the region of galactic latitudes of interest with overlapping model maps. For each map, the response to the map-averaged foreground was analyzed using the LRM method. This revealed that the minimum response is attained for a map centered at galactic coordinates $\ell = 13.7°$, $b = -74°$.

5. Conclusion

Next-generation experiments, both those that have already started collecting data and those planned for the future, can make a significant contribution to our understanding of the physics of the CMB and the early Universe. These include ground-based telescopes, space missions, and lunar observatory projects.

Currently, our knowledge of the CMB is limited to information on the angular power spectrum of the $\Delta T/T$ anisotropy and the approximate spectrum of the E-mode polarization. Furthermore, it has been roughly established that the random anisotropy field is essentially consistent with Gaussian statistics. In the era of high-precision cosmology, this helps estimate the most important parameters of the Standard Cosmological Model.

Still, many problems remain unresolved. As is well known, we are limited by so-called cosmic variance, i.e., the fact that we can only observe one last scattering surface and, with it, only one realization of the random process. This limits our knowledge of temperature fluctuations on large angular scales. Furthermore, the presence of large-scale anomalies in the observed anisotropy map and the quadrupole-octupole alignment require alternative sources of information unaffected by the noise of our Galaxy. Observing the anisotropic Sunyaev–Zel'dovich effect in nearby and distant galaxy clusters may help resolve this issue.

On the other hand, the power spectrum of the initial perturbations on small scales remains unknown. Such information is absent from both the large-scale structure of the Universe (due to the strong nonlinearity of gravitational processes) and the CMB anisotropy (due to Silk damping). Nevertheless, traces of small-scale perturbations remain in

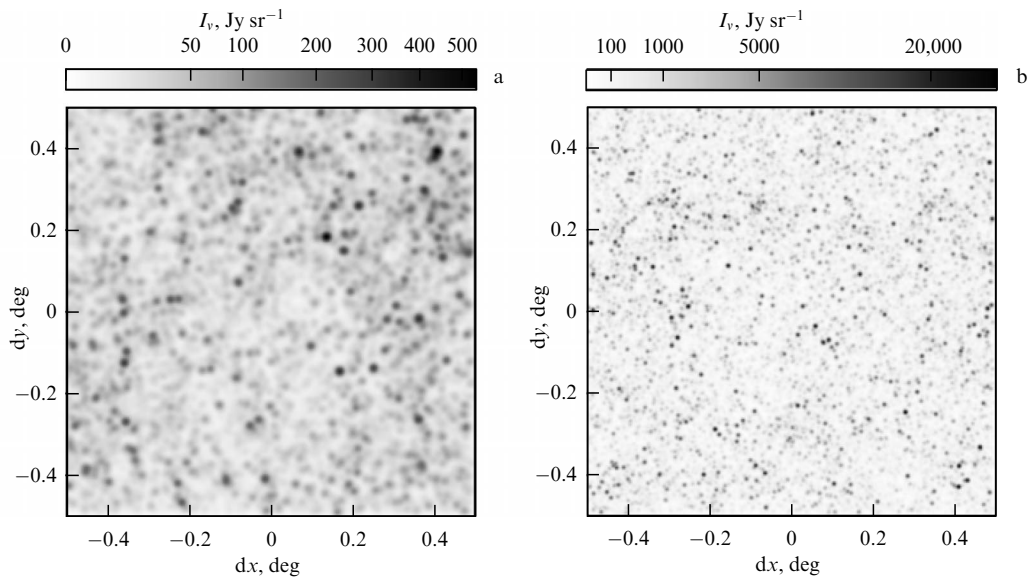

Figure 17. Examples of model sky maps in CO lines in 15-GHz-wide spectral channels at (a) 100 GHz and (b) 250 GHz.

the distortions of the frequency spectrum of the CMB radiation. This provides invaluable information about the inflationary stage of evolution.

The thermal history of the pre-recombination epoch is also unknown. The only information about it is can be available from μ-distortions. At the same time, y-distortions and relativistic corrections to them will provide valuable insights into the structure and physical properties of galaxy clusters and the history of reionization.

Finally, the existence of a primordial B-mode polarization, whose reliable detection would serve as evidence for the inflation hypothesis, has not yet been established.

Solving these problems requires not only next-generation experiments with greater sensitivity than currently available, combined with the selection of the least contaminated sky regions, but also appropriate approaches to processing observational data. Although signal-foreground separation methods such as the LRM offer the fundamental possibility of eliminating many foregrounds, proper modeling of their spectra and spatial correlation features is essential. Identifying the characteristic properties of components of the millimeter-wave signal observed, such as thermal emission from galactic dust, synchrotron radiation, free–free emission radiation, the CIB from distant galaxies, and the foreground from CO lines, both can help eliminate their contribution when observing polarization and spectral distortions in the CMB and is of significant scientific value for studying the physical properties of the objects generating this foreground radiation.

This study was supported by grant 24-22-00230 from the Russian Science Foundation, https://rscf.ru/project/24-22-00230/.

References

1. Bennett C L et al. *Astrophys. J. Suppl.* **208** 20 (2013)
2. Ade P A R et al. (Planck Collab.) *Astron. Astrophys.* **571** A15 (2014)
3. Ade P A R et al. (Planck Collab.) *Astron. Astrophys.* **536** A1 (2011)
4. Verkhodanov O V *Phys. Usp.* **59** 3 (2016); *Usp. Fiz. Nauk* **186** 3 (2016)
5. Abazajian K et al. (CMB-S4 Collab.) *Astrophys. J.* **926** 54 (2022)
6. Allys E et al. (LiteBIRD Collab.) *Prog. Theor. Exp. Phys.* **2023** 042F01 (2023) DOI: 10.1093/ptep/ptac150
7. Kogut A et al. *JCAP* **2011** (07) 025 (2011)
8. Tegmark M, Efstathiou G *Mon. Not. R. Astron. Soc.* **281** 1297 (1996)
9. Sudevan V et al. *Astrophys. J.* **842** 62 (2017)
10. Sazhin M V, Sironi G, Khovanskaya O S *New Astron.* **9** 83 (2004)
11. Hertig E et al. (Simons Observatory Collab.) *Phys. Rev. D* **110** 043532 (2024)
12. Yu B, Hill J C, Sherwin B D *Phys. Rev. D* **96** 123511 (2017)
13. BICEP/Keck Collab. Ade P A R et al. (BICEP/Keck Collab., SPTpol Collab.) *Phys. Rev. D* **103** 022004 (2021)
14. Namikawa T et al. *Phys. Rev. D* **105** 023511 (2022)
15. Starobinsky A A *Phys. Lett. B* **117** 175 (1982)
16. Matacz A *Phys. Rev. D* **56** R1836 (1997)
17. Desjacques V et al. *Mon. Not. R. Astron. Soc.* **451** 4460 (2015)
18. Chluba J, arXiv:1405.6938
19. Kurt V G, Shakhvorostova N N *Phys. Usp.* **57** 389 (2014); *Usp. Fiz. Nauk* **184** 423 (2014)
20. Mather J C et al. *Astrophys. J. Lett.* **354** L37 (1990)
21. Fixsen D J *Astrophys. J.* **707** 916 (2009)
22. Novikov I D et al. *Phys. Usp.* **64** 386 (2021); *Usp. Fiz. Nauk* **191** 404 (2021)
23. Likhachev S F, Larchenkova T I *Phys. Usp.* **67** 768 (2024); *Usp. Fiz. Nauk* **194** 814 (2024)
24. Kogut A et al., in *Space Telescopes and Instrumentation 2016: Optical, Infrared, and Millimeter Wave* (Proc. SPIE, Vol. 9904, Eds H A MacEwen et al.) (Bellingham, WA: SPIE, 2016) p. 99040W, DOI: 10.1117/12.2231090
25. Abitbol M H et al. *Mon. Not. R. Astron. Soc.* **471** 1126 (2017)
26. Kogut A et al. *JCAP* **2023** (07) 057 (2023)
27. Maillard J-P *Philos. Trans. R. Soc. A* **379** 20200212 (2021)
28. Edigaryev I G, Novikov D I, Pilipenko S V *Phys. Rev. D* **98** 123513 (2018)
29. Novikov D I et al. *Phys. Rev. D* **101** 123510 (2020)
30. Bevis N et al. *Phys. Rev. D* **76** 043005 (2007)
31. Bevis N et al. *Phys. Rev. D* **82** 065004 (2010)
32. Lizarraga J et al. *Phys. Rev. Lett.* **112** 171301 (2014)
33. Lizarraga J et al. *Phys. Rev. D* **90** 103504 (2014)
34. Durrer R, Figueroa D G, Kunz M *JCAP* **2014** (08) 029 (2014)
35. Moss A, Pogosian L *Phys. Rev. Lett.* **112** 171302 (2014)
36. Bonvin C, Durrer R, Maartens R *Phys. Rev. Lett.* **112** 191303 (2014)
37. Ortolan A, Lucchin F, Matarrese S *Phys. Rev. D* **38** 465 (1988)
38. Linde A, Mukhanov V *Phys. Rev. D* **56** R535 (1997)
39. Novikov D I, Parfenov K O, arXiv:2411.15959
40. Doroshkevich A G *Astrophysics* **6** 320 (1970); *Astrofizika* **6** 581 (1970)
41. Bardeen J M et al. *Astrophys. J.* **304** 15 (1986)
42. Bond J R, Efstathiou G *Mon. Not. R. Astron. Soc.* **226** 655 (1987)
43. Gott J R (III) et al. *Astrophys. J.* **352** 1 (1990)
44. Schmalzing J, Gorski K M *Mon. Not. R. Astron. Soc.* **297** 355 (1998)
45. Naselsky P D, Novikov D I *Astrophys. J.* **507** 31 (1998)
46. Zhao W *Res. Astron. Astrophys.* **14** 625 (2014)
47. Ganesan V et al. *JCAP* **2015** (02) 028 (2015)
48. Santos L, Wang K, Zhao W *JCAP* **2016** (07) 029 (2016)
49. Chingangbam P et al. *Phys. Lett. B* **771** 67 (2017)
50. Joby P K et al. *JCAP* **2019** (01) 009 (2019)
51. Kochappan J P et al. *Phys. Rev. D* **103** 123523 (2021)
52. Carones A et al. *Mon. Not. R. Astron. Soc.* **527** 756 (2024)
53. Luo X, Schramm D N *Phys. Rev. Lett.* **71** 1124 (1993)
54. Luo X *Astrophys. J. Lett.* **427** L71 (1994)
55. Akrami Y et al. (Planck Collab.) *Astron. Astrophys.* **641** A9 (2020)
56. Komatsu E, Spergel D N *Phys. Rev. D* **63** 063002 (2001)
57. Greco A, Bartolo N, Gruppuso A *JCAP* **2022** (03) 050 (2022)
58. Duivenvoorden A J, Meerburg P D, Freese K *Phys. Rev. D* **102** 023521 (2020)
59. Shiraishi M *Phys. Rev. D* **94** 083503 (2016)
60. Meerburg P D et al. *Phys. Rev. D* **93** 123511 (2016)
61. Bucher M, Racine B, van Tent B *JCAP* **2016** (05) 055 (2016)
62. Bartolo N, Liguori M, Shiraishi M *JCAP* **2016** (03) 029 (2016)
63. Luo X, Schramm D N *Astrophys. J.* **408** 33 (1993)
64. Khan M I, Saha R *JCAP* **2022** (06) 006 (2022)
65. Verkhodanov O V *Phys. Usp.* **55** 1098 (2012); *Usp. Fiz. Nauk* **182** 1177 (2012)
66. Novikov D, Feldman H A, Shandarin S F *Int. J. Mod. Phys. D* **8** 291 (1999)
67. Barreiro R B et al. *Mon. Not. R. Astron. Soc.* **296** 693 (1998)
68. Kotok E et al. *Int. J. Mod. Phys. D* **10** 501 (2001)
69. Vafaei Sadr A, Movahed S M S *Mon. Not. R. Astron. Soc.* **503** 815 (2021)
70. Ben-David A, Liu H, Jackson A D *JCAP* **2015** (06) 051 (2015)
71. Naselsky P D, Novikov D I *Astrophys. J. Lett.* **444** L1 (1995)
72. Novaes C P et al. *JCAP* **2015** (09) 064 (2015)
73. Novaes C P et al. *JCAP* **2014** (01) 018 (2014)
74. Dolgov A D et al. *Int. J. Mod. Phys. D* **8** 189 (1999)
75. Dolgov A D et al. *Astron. Astrophys. Trans.* **19** 213 (2000)
76. Novikov D I, Parfenov K O *Phys. Rev. D* **111** 063536 (2025)
77. Rybicki G B, Press W H *Astrophys. J.* **398** 169 (1992)
78. Challinor A D, Ford M T, Lasenby A N *Mon. Not. R. Astron. Soc.* **312** 159 (2000)
79. Maillard J-P et al. *Phys. Rev. D* **109** 023523 (2024)
80. Remazeilles M, Delabrouille J, Cardoso J-F *Mon. Not. R. Astron. Soc.* **418** 467 (2011)
81. Remazeilles M, Chluba J *Mon. Not. R. Astron. Soc.* **494** 5734 (2020)
82. Hill J C, Pajer E *Phys. Rev. D* **88** 063526 (2013)
83. Stolyarov V et al. *Mon. Not. R. Astron. Soc.* **357** 145 (2005)
84. Chluba J, Hill J C, Abitbol M H *Mon. Not. R. Astron. Soc.* **472** 1195 (2017)
85. Rotti A, Chluba J *Mon. Not. R. Astron. Soc.* **500** 976 (2021)
86. Górski K M et al. *Astrophys. J.* **622** 759 (2005)

87. Akrami Y et al. (Planck Collab.) *Astron. Astrophys.* **641** A7 (2020)
88. Blas D, Lesgourgues J, Tram T *JCAP* **2011** (07) 034 (2011)
89. Pen U-L *Astrophys. J.* **490** L127 (1997)
90. Aghanim N et al. (Planck Collab.) *Astron. Astrophys.* **641** A1 (2020)
91. Ade P A R et al. (Planck Collab.) *Astron. Astrophys.* **571** A28 (2014)
92. Akrami Y et al. (Planck Collab.) *Astron. Astrophys.* **641** A4 (2020)
93. Draine B T, Lee H M *Astrophys. J.* **285** 89 (1984)
94. Désert F-X *Astron. Astrophys.* **659** A70 (2022)
95. Adam R et al. (Planck Collab.) *Astron. Astrophys.* **594** A10 (2016)
96. de la Hoz E et al. *Mon. Not. R. Astron. Soc.* **519** 3504 (2023)
97. Fuskeland U et al. *Astrophys. J.* **790** 104 (2014)
98. Carretti E et al. *Mon. Not. R. Astron. Soc.* **489** 2330 (2019)
99. Shchekinov Yu A et al. *Phys. Usp.* **60** 961 (2017); *Usp. Fiz. Nauk* **187** 1033 (2017)
100. Lilly S J et al. *Astrophys. J. Lett.* **460** L1 (1996) DOI: 10.1086/309975
101. Franceschini A et al. *Mon. Not. R. Astron. Soc.* **310** L5 (1999)
102. Madau P, Dickinson M *Annu. Rev. Astron. Astrophys.* **52** 415 (2014)
103. Rowan-Robinson M et al. *Mon. Not. R. Astron. Soc.* **461** 1100 (2016)
104. Hauser M G, Dwek E *Annu. Rev. Astron. Astrophys.* **39** 249 (2001)
105. Lagache G, Puget J-L, Dole H *Annu. Rev. Astron. Astrophys.* **43** 727 (2005)
106. Dole H, Lagache G, Puget J-L *Astrophys. J.* **585** 617 (2003)
107. Pilipenko S V et al. *Astron. Lett.* **43** 644 (2017); *Pis'ma Astron. Zh.* **43** 715 (2017)
108. Ermash A A, Pilipenko S V, Lukash V N *Astron. Lett.* **46** 298 (2020); *Pis'ma Astron. Zh.* **46** 317 (2020)
109. Ermash A A et al. *Astron. Rep.* **65** 1194 (2021); *Astron. Zh.* **98** 980 (2021)
110. De Zotti G et al. *JCAP* **2016** (03) 047 (2016)
111. Decarli R et al. *Astrophys. J.* **902** 110 (2020)
112. Bernal J L, Kovetz E D *Astron. Astrophys. Rev.* **30** 5 (2022)
113. Carilli C L, Walter F *Annu. Rev. Astron. Astrophys.* **51** 105 (2013)
114. Silk J, Spaans M *Astrophys. J. Lett.* **488** L79 (1997)
115. Greve T R, Sommer-Larsen J *Astron. Astrophys.* **480** 335 (2008)
116. Goldreich P, Kwan J *Astrophys. J.* **189** 441 (1974)
117. Righi M, Hernández-Monteagudo C, Sunyaev R A *Astron. Astrophys.* **489** 489 (2008)
118. Lacey C, Cole S *Mon. Not. R. Astron. Soc.* **262** 627 (1993)
119. Mashian N, Sternberg A, Loeb A *JCAP* **2015** (11) 028 (2015)
120. Mashian N, Loeb A, Sternberg A *Mon. Not. R. Astron. Soc.* **458** L99 (2016)
121. Abitbol M H et al. *Mon. Not. R. Astron. Soc.* **471** 1126 (2017)
122. Greve T R et al. *Astrophys. J.* **794** 142 (2014)